

Accurate Modeling of Tagged CMR 3D Image Appearance Characteristics to Improve Cardiac Cycle Strain Estimation

Abstract. To reduce noise within a tag line, unsharpen the tag edges in spatial domain, and amplify the tag-to-background contrast, a 3D energy minimization framework for the enhancement of tagged Cardiac Magnetic Resonance (CMR) image sequences, based on learning first- and second-order visual appearance models, is proposed. The first-order appearance modeling uses adaptive Linear Combinations of Discrete Gaussians (LCDG) to accurately approximate the empirical marginal probability distribution of CMR signals for a given sequence, separate tag and background submodels. It is also used to classify the tag lines and the background. The second-order model considers image sequences as samples of a translation- and rotation-invariant 3D Markov-Gibbs Random Field (MGRF) with multiple pairwise voxel interactions. A 3D energy function for this model is built by using the analytical estimation of the spatiotemporal geometry and Gibbs potentials of interaction. To improve the strain estimation, by enhancing the tag and background homogeneity and contrast, the given sequence is adjusted using comparisons to the energy minimizer. Special 3D geometric phantoms, motivated by statistical analysis of the tagged CMR data, have been designed to validate the accuracy of our approach. Experiments with the phantoms and twenty real data sets have confirmed the high accuracy of the functional parameters that are estimated for the enhanced tagged sequences when using popular spectral techniques, such as spectral Harmonic Phase (HARP).

Keywords: Tagged CMR image, tag line, linear combination of Gaussians, Markov random field, appearance model

1 Introduction

Tagged Cardiac Magnetic Resonance Imaging (CMR) is a well-known technique for detailed and non-invasive visualization of myocardium motion and deformation [1]. Local diseases, such as coronary atherosclerosis, and global conditions, such as heart failure and diabetes, result in wall dysfunction that manifest on tagged images, with full 3D spatial geometric concordance. Cardiac, or MR, tagging, places a pre-specified pattern of temporary markers (called tags) inside soft body tissues, e.g. tag lines created by patterns of magnetic spin in the examined tissue, so that the motion in the tagged tissue can be measured from the images [2]. This technique complements traditional anatomical images and

can capture detailed information about the heart over time. While traditional MR techniques carry only information about the motion at the boundaries of an object, the tag lines allow us to examine the strain and displacement of the interior of the tissue in close detail [3].

Known methods for analyzing tagged MR images fall into the two broad spatial and spectral (frequency domain) categories. Spectral based techniques exploit the fact that harmonic phases of material points do not change with motion, and use this fact to build a tissue motion field [4, 5]. Spectral analysis techniques have become popular due to their speed, and in many cases, following a points' harmonic movement provides the more accurate tracking method. In this paper we focus on the well-established area of spectral analysis, e.g. the Harmonic Phase (HARP) method. The Harmonic Phase (HARP) method computes phase images from sinusoidal tagged MR images by bandpass filtering in the Fourier domain [4]. If the tissue in the area being tracked has a low temporal resolution or a high rate of movement, or if the MR tag parameters are selected incorrectly, this leads to corruption and noise in the acquired images. This results in spectral analysis methods failing to accurately track the tissue. More specifically, the primary causes of corruption and spectral based tracking failures can be classified into three types of causes [2]: a high rate of motion between two successive frames, a through-plane motion, and boundary point tracking.

Spectral tracking failures that result from noise and data corruption, often require the user to manually identify and correct mistracked points [6], and in some cases manual adjustments may be required for multiple data points in every image in a sequence. This process is very time-consuming, especially in studies or clinical examinations when large numbers of data points must be tracked. Because optimally tagged CMR images are difficult to obtain, effective image refinement and correction techniques are of prime and urgent necessity in the field of CMR imaging.

Several techniques have been proposed to directly improve tagged MR images. For example, Yang and Murase [1] proposed a technique to improve tagged MR images based on contrast enhancement and texture analysis using histogram modification. In a continuation of the first paper, Yang and Murase [7] use a refined method that incorporates additional filtering before applying the histogram equalization. To recover missing data found between tag lines Yuan et al. [8] proposed an approach for the implementation of a complex bandpass filter using wavelet decomposition. While this technique did provide enhancement to the taglines, it was computationally difficult to efficiently employ the algorithm.

The majority of the known techniques focus on (i) improving either the spectral tracking directly, which makes compatibility with existing commercial spectral frameworks difficult; (ii) improving the contrast of tag lines in spatial images, which does not reliably enhance their spectral qualities to improve spectral tracking; (iii) they require user input, which can be quite time consuming, and (iv) they required prior knowledge about the data set, which can be difficult to acquire in clinical environments. Also, the known techniques that directly modify the images are computationally expensive, making their practical imple-

mentation difficult. To address the problem of tagged MR image refinement we propose a more practicable energy minimization based approach for improving the tagged CMR images directly.

2 Image Refinement: Models and Methods

Basic notation. Let $\mathbf{r} = (x, y, t)$ and $\mathbf{R} = [(x, y, t) : x = 0, \dots, X - 1; y = 0, \dots, Y - 1, t = 0, \dots, T - 1]$ denote a 3D point, or voxel with two spatial (x, y) and one time (t) coordinates and a spatiotemporal lattice of the size XYT , respectively. Let $\mathbf{Q} = \{0, \dots, Q - 1\}$ be a finite set of signals (i.e., gray levels intensities). The lattice \mathbf{R} supports 3D CMR image sequences $\mathbf{g} = [g(x, y, t) : (x, y, t) \in \mathbf{R}; g(x, y, t) \in \mathbf{Q}]$, consisting of 2D MR slices taken in successive time instants.

We describe visual appearance of the tagged CMR images with a 1st-order model of marginal probability distributions of tag and background signals and a 2nd-order model of characteristic voxel-wise and pairwise voxel signal dependencies.

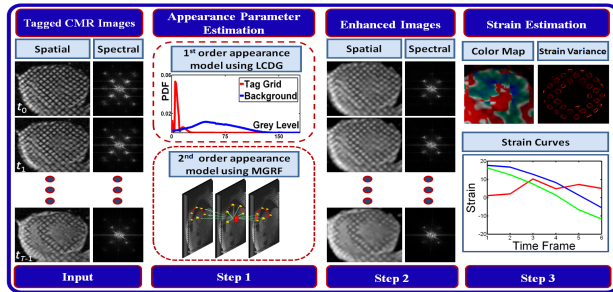


Fig. 1. Block-diagram of the proposed refinement of tagged MR images.

2.1 The 2nd-Order MGRF Appearance Model

A translation- and rotation-invariant generic second-order MGRF of images \mathbf{g} is specified by a certain number, N , of characteristic central-symmetric voxel neighborhoods \mathbf{n}_ν ; $\nu = 1, \dots, N$, on \mathbf{R} shown in Fig. 2. Each neighborhood \mathbf{n}_ν indicates a family of voxel pairs, $\mathbf{C}_\nu = \{\mathbf{c}_\nu = (\mathbf{r}, \mathbf{r}') : \mathbf{r}' - \mathbf{r} \in \mathbf{n}_\nu; \mathbf{r}, \mathbf{r}' \in \mathbf{R}\}$, such that the inter-voxel distances (norms of the coordinate offsets $\mathbf{o} = \mathbf{r}' - \mathbf{r}$) belong to an indexed semi-open interval $[d_{\nu:\min}, d_{\nu:\max}]$:

$d_{\nu:\min} \leq \sqrt{(x - x')^2 + (y - y')^2 + (t - t')^2} < d_{\nu:\max}$. with the fixed thresholds $d_{\nu:\min}$ and $d_{\nu:\max}$. These neighboring pairs are considered as second-order cliques of the neighborhood graph with nodes in the voxels. Cliques from the family \mathbf{C}_ν



Fig. 2. Central-symmetric 2nd-order 3D neighborhood system for a voxel.

support the same real-valued Gibbs potential $V_\nu(g(\mathbf{r}), g(\mathbf{r}'))$ of pairwise voxel interaction. To uniformly account for contrast, the potential depends on the absolute intra-clique signal difference: $\Delta = |g(\mathbf{r}) - g(\mathbf{r}')| \in \mathbf{D} = \{0, 1, \dots, Q - 1\}$. The potential values can be represented as a vector $\mathbf{V}_\nu = [V_\nu(\Delta) : \Delta \in \mathbf{D}]^\top$

where \top indicates the transposition. The characteristic cliques to be taken into account in the MGRF are stratified into N families, $\{\mathbf{C}_\nu : \nu = 1, \dots, N\}$, with the potentials \mathbf{V}_ν and non-intersecting distance intervals: $d_{1:\min} < d_{1:\max} \leq d_{2:\min} < \dots \leq d_{N:\min} < d_{N:\max}$. Such an MGRF has the Gibbs probability distribution [9]: $P(\mathbf{g}) = \frac{1}{Z} \exp \left(|\mathbf{R}| \left(\mathbf{V}_{\text{vox}}^\top \mathbf{F}(\mathbf{g}) + \sum_{\nu=1}^N \rho_\nu \mathbf{V}_\nu^\top \mathbf{F}_\nu(\mathbf{g}) \right) \right)$ where Z is the normalizing factor (the partition function) depending on the potentials $\mathbf{V} = [\mathbf{V}_{\text{vox}}; \mathbf{V}_\nu : \nu = 1, \dots, N]$ and the neighborhoods $\{\mathbf{n}_\nu : \nu = 1, \dots, N\}$, and $\rho_\nu = \frac{|\mathbf{C}_\nu|}{|\mathbf{R}|}$ is the relative size of the clique family with respect to the lattice cardinality $|\mathbf{R}| = XYT$, i.e., the relative number of cliques in the family \mathbf{C}_ν . The vectors $\mathbf{F}(\mathbf{g})$ and $\mathbf{F}_\nu(\mathbf{g})$ contain relative empirical frequencies $f(q|\mathbf{g})$ of signals $q \in \mathbf{Q}$ in the voxels and frequencies $f_\nu(\Delta|\mathbf{g})$ of absolute signal differences $\Delta \in \mathbf{D}$ in the cliques from the family \mathbf{C}_ν for the image \mathbf{g} , respectively: $\mathbf{F}(\mathbf{g}) = f(\mathbf{g}) = \frac{|\mathbf{R}_q(\mathbf{g})|}{|\mathbf{R}|}; \sum_{q \in \mathbf{Q}} f(q|\mathbf{g}) = 1$ and $\mathbf{F}_\nu(\mathbf{g}) = f_\nu(\Delta|\mathbf{g}) = \frac{|\mathbf{C}_{\nu:\Delta}(\mathbf{g})|}{|\mathbf{C}_\nu|}; \sum_{\Delta \in \mathbf{D}} f_\nu(\Delta|\mathbf{g}) = 1$ where the sublattice $\mathbf{R}_q(\mathbf{g})$ contains all the voxels \mathbf{r} , such that $g(\mathbf{r}) = q$ and the subfamily $\mathbf{C}_{\nu:\Delta}(\mathbf{g})$ contains all the cliques $\mathbf{c}_\nu = (\mathbf{r}, \mathbf{r}')$ of this family, such that $|g(\mathbf{r}) - g(\mathbf{r}')| = \Delta$.

Analytical first approximations of the maximum likelihood estimates of the potentials are as follows (see supplementary material for the detailed analytical proof): $V_{\text{vox}}(q) = \lambda (f(q|\mathbf{g}) - f_{\text{irf}}(q)); q \in \mathbf{Q}$; $V_\nu(\Delta) = \lambda (f_\nu(\Delta) - f_{\text{irf}}(\Delta)); \Delta \in \mathbf{D}; \nu = 1, \dots, N$ where the common scaling factor λ is also computed analytically, and $f_{\text{irf}}(q) = \frac{1}{Q}$ and $f_{\text{irf}}(\Delta)$ denote the probability of the signal q and the inter-voxel signal difference Δ , respectively, for the independent random field of equiprobable signals: $f_{\text{irf}}(\Delta) = \begin{cases} \frac{1}{Q} & \text{if } \Delta = 0 \\ \frac{2(Q-\Delta)}{Q^2} & \text{otherwise} \end{cases}$ The factor λ can be omitted ($\lambda = 1$) if only relative interaction energies $E_{\text{rel}:\nu}$ are computed for the clique families to select the most characteristic ones.

2.2 The 1st-Order LCDG Appearance Model

A discrete Gaussian (DG) $\Psi_\theta = (\psi(q|\theta) : q \in \mathbf{Q})$ is defined [10] as a discrete probability distribution with Q components obtained by integrating a continuous 1D Gaussian density $\varphi(q|\theta) = (\sigma * \sqrt{2\pi})^{-1} * \exp \left(-\frac{(q-\mu)^2}{2\sigma^2} \right)$ with parameters $\theta = (\mu, \sigma)$, where μ is the mean and σ^2 is the variance, over Q intervals related to the successive signal values in \mathbf{Q} : if $\Phi_\theta(q) = \int_{-\infty}^q \varphi(z|\theta) dz$ is the cumulative Gaussian probability function, then $\psi(0|\theta) = \Phi_\theta(0.5)$, $\psi(q|\theta) = \Phi_\theta(q + 0.5) - \Phi_\theta(q - 0.5)$ for $q = 1, \dots, Q - 2$, and $\psi(Q - 1|\theta) = 1 - \Phi_\theta(Q - 1.5)$.

To enhance the tag-to-background contrast, the empirical marginal 1D signal distribution for the CMR image to be refined is accurately approximated with a Linear Combination of Discrete Gaussians (LCDG) $\mathbf{P}_{\mathbf{w}, \Theta} = [p_{\mathbf{w}, \Theta}(q) : q \in \mathbf{Q}]$; $\sum_{q \in \mathbf{Q}} p_{\mathbf{w}, \Theta}(q) = 1$, with two positive dominant and multiple sign-alternate subordinate DGs: $p_{\mathbf{w}, \Theta}(q) = \sum_{k=1}^{K_p} w_{p:k} \psi(q|\theta_{p:k}) - \sum_{l=1}^{K_n} w_{n:l} \psi(q|\theta_{n:l})$ where K_p ; $K_p \geq 2$, and K_n ; $K_n \geq 0$, are total numbers of the positive and negative DGs, and $\mathbf{w} = [w_{p:k}, w_{n:l}]$ are the non-negative weights that meet the obvious con-

straint $\sum_{k=1}^{K_p} w_{p,k} - \sum_{l=1}^{K_n} w_{n,l} = 1$. The subordinate DGs approximate closely the deviations of the empirical distribution from the conventional mixture of the dominant positive DGs.

2.3 Energy Minimization to Enhance Tagged CMR Images

We adjust a tagged CMR image \mathbf{g} by searching with the voxel-wise Iterative Conditional Mode (ICM) relaxation for a local minimum of the Gibbs energy function for the second-order MGRF appearance model:

$\hat{\mathbf{g}} = \arg \min_{\mathbf{g} \in \mathbf{Q}^{XYT}} \left\{ \mathbf{V}_{\text{vox}}^T \mathbf{F}(\mathbf{g}) + \sum_{\nu=1}^N \rho_\nu \mathbf{V}_\nu^T \mathbf{F}_\nu(\mathbf{g}) \right\}$ where the probability vectors $\mathbf{F}_{\text{vox}}(\mathbf{g})$ and $\mathbf{F}_\nu(\mathbf{g})$ are collected over the generated tagged CMR image sequence. To enhance the tag-background contrast, each estimated signal value $\hat{g}(\mathbf{r})$; $\mathbf{r} \in \mathbf{R}$, is classified as belonging to either the tag line or the background by using the first-order LCDG modelling. Then the voxels are nudged towards their proper grouping by incrementing or decrementing their signals by a small value δ in accord with the discriminant threshold, τ .

3 Experimental Results

The effectiveness of the proposed approach was tested on both synthetic phantom images and in-vivo data by analyzing the strain of the data sets using the HARP technique and quantifying the performance with the indexes: (*i*) the ability to restore strain slopes for synthetic phantoms, (*ii*) the homogeneity of the strain variance in the data, and (*iii*) the relative power scatter between the main and side spectral lobes.

Validation on Synthetic Phantoms: The synthetic phantoms were constructed using a descriptive mathematical model [11] that accounts for physiological features and the left ventricle (LV) response during the cardiac cycle. To obtain the phantoms, a motion transformation is applied to a generated 3D LV model and images are generated at an intersecting plane. A phantom constructed using this model is exemplified in Fig. 3 (a). Realistic images are simulated by corrupting the phantom images with Gaussian noise using the signal-to-noise Ratios (SNR) of 3.18 dB and 2.58 dB, as shown in Fig. 3 (b) and (c), respectively. In cardiac strain analysis, the slope of the contraction phase of

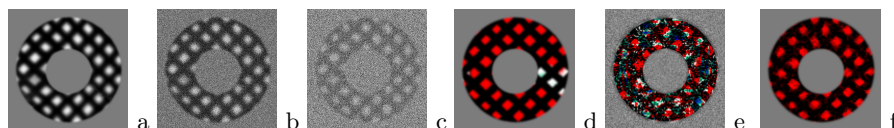


Fig. 3. Original phantom (a) and two Gaussian corruption levels with the SNR of 3.18 dB (b) and 2.58 dB (c). Visualization of the strain on the phantom for the original (d), corrupted (e) and enhanced (f) images. Coloring indicates the strain percentage. Note how the strain is largely recovered in the enhanced image.

the cardiac cycle is a very important part of the strain curve, i.e., cardiac systolic performance index, or rate of peak contraction. Therefore, the accurate recovery of this slope is an important index of a tagged MR restoration algorithm. To measure the effect of the additive noise on the calculated strain, the absolute strain error, i.e., the difference between the slopes of the noisy data analyzed

and the ground truth, was calculated for the phantom images, using the HARP technique and the Euler strain measurements. The absolute strain error for the noisy phantom images has been reduced after the proposed processing from 94% to 35.7%. Figure 3 (d-f) visually compares the strain in the original, corrupted, and enhanced phantom images.

The actual strain slopes calculated for the original, noisy, and our enhanced phantoms are compared in Fig. 4. As is expected and demonstrated in Fig. 4, the strain values are decreasing linearly with time during the contraction phase of the cardiac cycle. That the slope profiles for the enhanced and ground truth images are very similar clearly demonstrates the capabilities of the proposed approach to facilitate the accurate recovery of the strain slopes for the tagged MR data. Visually this is also evident from the color uniformity of the images in Fig. 3, (d) and (f). At the same time, the color scatter over the noisy phantom in Fig. 3, (e), illustrates the failure of the HARP-based strain calculations under the large corrupting noise. For accurate computations in the spectral domain, the

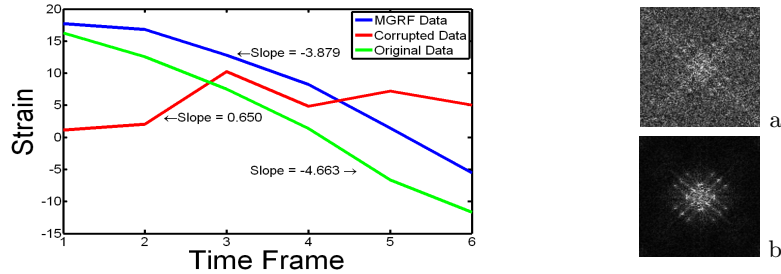


Fig. 4. Strains calculated at the contraction phase of the cardiac cycle for the original, corrupted, and enhanced phantom images. The slope is made unreliable in the corrupted phantom, indicating that the HARP analysis cannot track the strain. After our enhancement the slope, is largely recovered.

HARP technique requires that the information reside predominately within the central peak and first side lobes. The Fourier spectral representations of the noisy and enhanced phantom images in Fig. 5 justify the high accuracy of recovering the strain slope using the proposed approach. As shown in Fig 5 (a), it is the increased power scatter distributing information in the outer side lobes of the Fourier domain for the noisy phantom image that greatly affects the accuracy of the HARP analysis [12].

On the contrary, our enhancement reduces the scatter in the outer side lobes and emphasizes the main lobe and first side lobes in the Fourier image spectral domain, which therefore makes the HARP analysis much more accurate. In total, our approach gives $265\% \pm 20\%$ of noise reduction in the side lobes of the phantom image spectrum. Table 1 summarizes the noise reduction results for the phantom data.

Another important aspect of the proposed approach is the ability to restore strain homogeneity in the tagged MR images, which is directly related to the ability to restore the strain slopes (the improved homogeneity leads to the im-

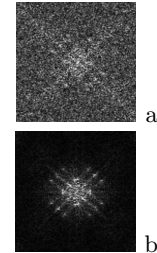


Fig. 5. Fourier spectra of the noisy (a) and enhanced (b) phantom images. The noise in the processed phantom spectra (b) is reduced from the noisy phantom spectra (a).

proved strain slope). Based on biomechanical models of the heart tissue as a continuous material, neighboring voxels in a heart should have similar strains, and the strain does not randomly occur in every individual voxel, the variance in strain (homogeneity) in actual tagged MR image sequences should be low[13]. This should hold true in any given continuous region, even in the presence of injury. To justify our approach, after the strains of each image were extracted, the strain homogeneity of the phantoms was calculated in terms of the strain variance in 7×7 windows across the phantom images. Differences between the mean strain homogeneity in Table 2 before and after the image enhancement are statistically significant by the unpaired *t*-test, so that our approach robustly improves both the strain slope and homogeneity. To illustrate this result, pixel-

Spectral Ratio	Before	After	Before	After
	Phantom	In-vivo		
Mean	0.17	0.58	1.40	2.04
St.dev.	0.012	0.019	0.19	0.31
% mean imp.	265%	45.52%		

	Before	After
Mean	0.024	0.0092
St.dev.	$2.9 \cdot 10^{-14}$	$1.8 \cdot 10^{-15}$
P-Value	$< 10^{-4}$	

Table 1. Showing the ratio of the main lobe's spectral power for the phantom and in-vivo data before (noisy) and after processing, with the percentage of improvement.

Table 2. Phantom strain homogeneity before and after processing.

wise parametric (color-coded) maps in Fig. 6 for the original, noisy, and enhanced phantoms are used to help visually assess the improvement in the strain homogeneity: the brighter the area, the larger the local strain variance. Our approach largely recovers the strain variance profile of the original image.

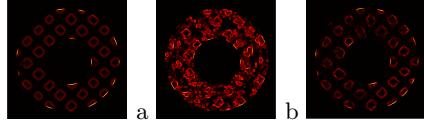


Fig. 6. Color strain variance maps for the original (a), noisy (b), and enhanced (c) phantom. The corrupted image shows increased variance and less discrete elements. Brighter area means larger strain variance.

Results for In-vivo Data: To test the realistic performance, the proposed approach has been applied to twenty in-vivo data sets. Shown in Fig. 7 (a-d), the results before and after enhancing one of the test images are similar to those for the phantom data, and the spectra shows a considerable noise reduction in the side lobes; see Fig. 7 (c) and (d). As shown in Table 1, the proposed approach

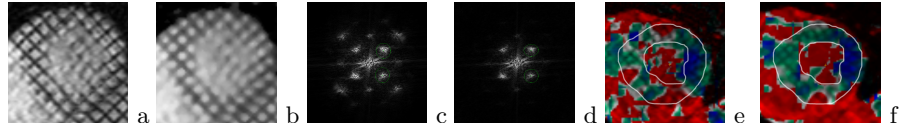


Fig. 7. An in-vivo data set: the original spatial (a) and processed (b) images and their Fourier spectra (c), (d). The spectral noise is notably reduced by the proposed image enhancement. In-vivo data strain maps before (e) and after (f) our enhancement. Note that the variability in strain has been largely reduced and the final homogeneity is notably increased.

can significantly reduce various levels of the noise, e.g., the noise reduction of

$42.6\% \pm 9.3\%$ in the spectral side lobes for all the twenty in-vivo data sets that take part in these experiments. Furthermore, similarly to the phantom data, the overall strain homogeneity of the image clearly increases as well. Figure 7 (e,f) demonstrates the color strain maps for an in-vivo image before and after the proposed enhancement, showing improved continuous areas.

Computational Efficiency: The processing time of the entire HARP analysis is only slightly increased with the proposed approach taking only 9.4 ± 0.2 seconds for a typical tagged MR image, and unlike other alternatives, our technique requires no user input or apriori model templates, helping to eliminate possible human errors.

4 Conclusion

Our LCDG and MGRF based modeling of the tagged MR images in the spatiotemporal domain is capable of recovering strain slopes, improving the main-to-side-lobe ratio in the Fourier spectra, and improving the strain homogeneity of the image. These image improvements ensure a more efficient and robust estimation of functional parameters with the today's spectral tools. In total, our approach adds only a minimal amount of time to HARP image analysis and leads to more accurate clinical cardiac measurements and evaluations, which provides clinicians with more accurate image data

References

1. X. Yang and K. Murase, "Tagged cardiac mr image segmentation by contrast enhancement and texture analysis," in *IEEE ICEMI*, pp. 4–210 –4–214, Aug 2009.
2. X. Liu and J. Prince, "Shortest path refinement for motion estimation from tagged mr images," *IEEE TMI*, vol. 29, no. 8, pp. 1560 –1572, Aug 2010.
3. L. Axel and L. Dougherty, "MR imaging of motion with spatial modulation of magnetization," *Radiology*, vol. 171, pp. 841–845, Jun 1989.
4. N. F. Osman and J. L. Prince, "Visualizing myocardial function using HARP MRI," *Phys Med Bio*, vol. 45, pp. 1665–1682, Jun 2000.
5. B. A. Venkatesh, *et al.*, "Three-dimensional plus time biventricular strain from tagged MR images by phase-unwrapped harmonic phase," *J of Magn Reson Im*, vol. 34, pp. 799–810, Oct 2011.
6. X. Liu, E. Murano *et al.*, "Harp tracking refinement using seeded region growing," in *IEEE ISBI*, pp. 372 –75, April 2007.
7. X. Yang and K. Murase, "A multi-scale phase-based optical flow method for motion tracking of left ventricle," in *IEEE iCBBE*, pp. 1–4, June 2010.
8. X. Yuan, *et al.*, "A multiresolution method for tagline detection and indexing," *IEEE ITiB*, vol. 14, no. 2, pp. 507 –513, Mar 2010.
9. G. Gimel'farb, *Image textures and Gibbs random fields*. Kluwer Academic Pub, 1999, vol. 16.
10. A. El-Baz and G. Gimel'farb, "Em based approximation of empirical distributions with linear combinations of discrete gaussians," in *IEEE ICIP*, vol. 4, pp. 373–376, Oct 16-19 2007.
11. E. Waks, J. Prince *et al.*, "Cardiac motion simulator for tagged mri," in *IEEE MMBIA*, , pp. 182 –191, Jun 1996.
12. K. Hansen, F. Gran *et al.*, "In-vivo validation of fast spectral velocity estimation techniques," *Ultrasonics*, vol. 50, no. 1, pp. 52 –59, 2010.
13. K. B. Chandran, *et al.*, *Image-Based Computational Modeling of the Human Circulatory and Pulmonary Systems*. Springer, 2010.